




# Instabilities in the formation of single tracks during selective laser melting process

Samia Aggoune<sup>1</sup> · Farida Hamadi<sup>1</sup> · Cherifa Abid<sup>2</sup> · El-Hachemi Amara<sup>1</sup> · Parveen Kumar<sup>3</sup> · Ajay Kumar<sup>4</sup> 

Received: 3 December 2023 / Accepted: 25 April 2024

© The Author(s), under exclusive licence to Springer-Verlag France SAS, part of Springer Nature 2024

## Abstract

The selective laser melting process is recognized as a high-potential additive manufacturing process for complex metallic parts. However, during manufacturing, the occurrence of porosities, ripples and humps can affect the surface quality of the parts. To avoid these defects coming from the melt pool instabilities, it appears to be important to understand all the phenomena that occur during the process. The aim of this study is to avoid the appearance of the melt pool instabilities. For this reason, numerical investigation was performed using a computational fluid dynamics approach on the 316L stainless steel material. We considered fixed laser power, beam radius, and powder bed thickness (130 W, 60  $\mu\text{m}$ , 40  $\mu\text{m}$ ), and we reported the influence of varying the scanning speed (0.7, 0.9, 1.3, 1.5, 1.7, 1.9, and 2.0 m/s) on the quality of the solidified tracks and on the appearance of the dynamic instabilities. Our main results showed the occurrence of periodic humps at higher laser scanning speeds and ripples at lower ones. To prevent their occurrence, we found a suitable scanning speed leading to a stable state, which is observed at the transition between these two instabilities. Finally, our study allowed us to conclude that, neither Marangoni convection nor recoil pressure are at the origin of the appearance of ripples and humps.

**Keywords** Selective laser melting process · Fusion · Solidification · Instability · Morphology · Fluid dynamic

## 1 Introduction

Additive manufacturing is an advanced technology which produces complex parts based on computer-aided models. The latest developments in this field are assisted by artificial intelligence for different materials. Several studies [1–6] summarize the role of artificial intelligence in additive manufacturing. This approach explores smart materials to advance in biomedical engineering and industrial applications. It provides for nanomaterials and materials with high-quality properties. It also offers a detailed description of

several manufacturing techniques such as 3D and 4D printing. It discusses process modeling and gives methods for improving the characteristics of the materials manufactured as well as the means for developing the products obtained in a reduced time. These studies explain how smart materials present challenges related to sustainability, reparability and recyclability. Currently, the companies are being pushed to implement smart manufacturing practices, to obtain better productivity, at lower cost and with high precision.

The selective laser melting process is one of the processes of additive manufacturing; it allows the manufacture of three-dimensional objects layer by layer from a powdery material. This technique uses a laser to selectively heat and melt powder beds. It allows the fabrication of designed aerospace, biomedical and many other engineering parts, directly from computer-aided design, on the basis of CAD/CAM principles [7–10] using metal powders.

Its main advantage is to produce complex parts in a short time and with low material loss, although the main drawback of this process is its poor and inefficient surface finishing in some cases. Indeed, the surface morphology may contain porosity, adhered particles, undercuts, humps, ripple patterns

✉ Ajay Kumar  
ajay.kumar30886@gmail.com

<sup>1</sup> Laser Material Processing Team, Center for Development of Advanced Technologies, CDTA, PO. Box 17, 16 303 Baba-Hassen, Algiers, Algeria

<sup>2</sup> CNRS, IUSTI, Aix Marseille Univ, Marseille, France

<sup>3</sup> Department of Mechanical Engineering, Rawal Institute of Engineering and Technology, Faridabad, Haryana 121004, India

<sup>4</sup> Department of Mechanical Engineering, School of Engineering and Technology, JECRC University, Jaipur, Rajasthan, India

and other defects [11–13]. These surfaces need finishing by machining or coating [14].

Some investigations are developed to analyze the effects of the parameters on the characteristics of the produced parts. We must emphasize that the conducted researches are extensive and cover different aspects such as laser scanning strategies, mechanical properties, and powder nature, among others. Few researchers have examined the dynamics and the morphology of the liquid, among them, Zhang et al. [15], who analyzed the effects of convective and conductive heat flux on molten pool shape during the process of the aluminum alloy with a fixed heat Gaussian source. Their simulation results showed the dominance of the Marangoni convection, which accelerates the liquid metal flow outward; this makes the molten pool wider. They discuss the metallurgical defects due to several instabilities, such as balling instability, which can be reduced by preheating the substrate and by re-melting the powder. As for Kempen [16], he combined different laser powers and scanning speeds to determine the optimal scanning strategy and hatch spacing. He also tries to eliminate cracks by the use of pre-heating the base plate and re-melting the powder these are another devices to increase the part density and avoid roughness significantly. Further researches were carried out to investigate the mesoscopic features occurring during selective laser melting (SLM) processes. Several authors like [17, 18] describe the melting and solidification stages using the ALE multiphysics code and different laser powers. On the other hand, simulations advantages are the identification of the proper parameters without conducting expensive experimental testing. All these studies showed that the SLM process is complex and involves a combination of many different physical phenomena. Some of these phenomena are, melting, eventual vaporization, natural and Marangoni convection, wetting, balling, and instabilities due to fluctuations of the melt pool [19].

In what follows, we will focus on the occurrence of melt pool instabilities. Zhou et al. [20] suggested that the formation of surface defects in tungsten material during the SLM process could be attributed to melt pool instabilities, including oscillations from capillary convection, pulsed laser recoil pressure, and shear stress at the gas–melt interface. They attributed the balling to an incomplete wetting and to the high surface tension and viscosity of melted tungsten. As for Sun et al. [21], they carried out an experimental work, where they found that, the laser power has a major impact on the stability of the Ti6Al4V melt pool and its morphology. In fact, excessive scanning speed or insufficient laser power leads to balling and melt pool instability. This result was supported by Chen et al. [22], who studied numerically using a 3D finite difference method to predict the behavior of the molten K418 powder irradiated by a Gaussian beam. Their results showed that the reduction in the speed of the laser was beneficial to reduce the balling phenomenon, which is mainly due to the

absence of wetting effect. Zhang et al. [23], interested to the metallurgical defects on the SLM processing of aluminum alloys. They also proved that substrate preheating and laser re-melting could reduce the defects originating from balling instability.

Typically, humps and ripples are morphologies that can appear on the scan track at different input energy densities or different scan speeds. Gecys et al. [24] studied the influence of laser frequency on the ripple formation; they found that these ripples depend on the stainless steel material properties as well as on the used experimental conditions, such as the laser wavelength and spot diameter. They are also caused by the temperature gradient of the heat source. However, the study of Kou et al. [25] in welding of the 304 stainless steel showed that these ripples appear when the content of the surface-active agent is low. Which means the surface tension coefficient tends to be negative, this leads to drive the molten liquid outward (Marangoni force), thus ripples appear where disturbance occurs. As for Yang et al. [26], their study aims to reduce the surface roughness obtained on the produced AISi10Mg parts. They found that with an increase in energy density, the structure of the “ripples” gradually changed from a “tapered” to a “circular” pattern. Moreover, based on a numerical simulation method, and using the finite volume method and discrete element method, Wang et al. [27] discovered that the ripples became more and more intense due to the greater gradient temperature and surface tension caused by the Marangoni force and the increase in laser power. The same observation is given by the work of Mumtaz et al. [28], who used Nd: YAG pulsed laser to fabricate thin pieces with minimum roughness. They demonstrated that the ripple formation affects highly the roughness of their top surfaces.

The other instability, which has been intensively studied in laser welding, is the humping phenomenon. This one can also appear in the SLM process, when lateral surface tensions are applied on a thin melt-pool flow, they will provoke a periodic shrinking effect [29]. Based on an experimental method, Gunenthiram et al. [30], observed with a fast camera analysis humps during the SLM process of 316L stainless steel. They attributed this phenomenon to a large ratio of length to width of the molten pool that generated Plateau–Rayleigh instabilities. The work of Seiler et al. [31] shows that during a laser micro-welding process two regimes are obtained, a pre-humping regime with an elongated keyhole which leads to a wavy surface followed by a humping regime leading to deep grooves. In fact, periodic undulation exists at high laser speed, where an elongated melt pool is more susceptible to capillary instability. It is believed that poor wettability and the resulting large contact angle between the molten track and the substrate also contribute to this instability [32, 33]. It should be noted that the studies of the formation of these phenomena remain insufficient; there are still some gaps to be clarified. In Table 1, we have summarized the main works related to

**Table 1** Summary of the main literature studies on SLM instabilities and the highlight of our contribution

Author's (year)	SLM Instabilities
Zhou et al. (2015)	Balling effect is due to an incomplete wetting and to the high surface tension and viscosity of melted tungsten
Sun et al. (2013)	Balling instability of melted Ti6Al4V is due to excessive scanning speed or insufficient laser power
Chen et al. (2018)	Balling instability of melted K418 is due to the Plateau-Rayleigh instability and the absence of wetting effect
Zhang et al. (2019)	Balling instability of the molten aluminum alloy can be reduced by preheating the substrate and by re-melting the powder
Gecys et al. (2015)	Ripples formation depends on the stainless steel material properties as well as on the experimental conditions such as laser wavelength, pulse duration, polarization and the temperature gradient of the heat source
Kou et al. (2011)	Surface active-agent and the oscillatory Marangoni flow could affect the pool surface and lead to the ripples formation
Yang et al. (2019)	The structure of the AlSi10Mg ripples is related to the linear laser density. These ripples change from a "tapered" pattern to a "circular" pattern with an increase in energy density
Wang et al. (2019)	The Marangoni force and the increase of laser power lead to ripples when the laser power is very intense. The number of these ripples increases when the laser power becomes higher
Antony et al. (2014)	Humping instability appears when lateral surface tensions are applied on a thin melt-pool flow (periodic shrinking effect) during evaporation
Gunenthiram et al. (2017)	Humping effect is attributed to a large ratio of length to width of the molten pool during evaporation
Seiler et al. (2016)	Humps are observed during the formation of a keyhole and they are related to the recoil pressure. There are two regimes: prehumping and humping
Gusarov et al. (2010), King et al. (2015)	Humping instability observed during evaporation (recoil pressure) is due to a poor wettability and to the resulting large contact angle between the molten track and the substrate

**Table 1** (continued)

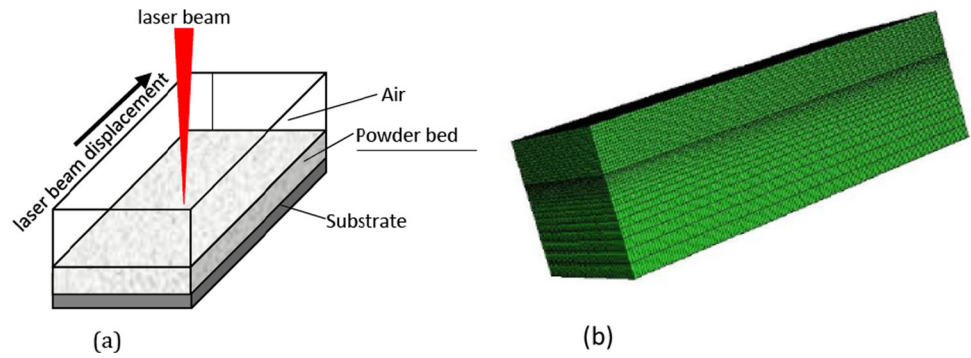
Author's (year)	SLM Instabilities
This study	The two instabilities (ripples and humps) are observed in the conduction mode and so, they are not systematically linked to the recoil pressure and evaporation We have concluded that, neither Marangoni convection nor recoil pressure are at the origin of the appearance of ripples and humps as expected by many researchers [24, 25, 27, 29–33] For a fixed laser power (130W), ripples are observed at low scanning speed and humps at the higher ones The transition from ripples to humps is a stable state observed at 1.5 m/s when the Marangoni convection is neglected, and at 2.0 m/s, when the Marangoni convection is included We believe that, when the normal component of the surface tension force is much greater than the shear forces due to the liquid metal viscosity, ripples can arise The heights of the ripples decrease with the increase of the scanning speeds The pre-humping regime presents elongated humps compared to those of the humping regime This study can prevent the occurrence of these two instabilities (ripples and humps) by choosing a suitable scanning speed ( $V = 2.0$ m/s when Marangoni convection is introduced and 1.5 m/s when it is neglected)

the instabilities that appeared during the SLM process, and we have included our own contribution while specifying their origins.

Although the selective laser melting of the 316L stainless steel process has been widely studied, due to its wide range of applications in the industry and its outstanding combination of good corrosion and high strength at high temperatures. The parts obtained by SLM are different to those obtained by traditional processes because of highly located heat inputs, very short interaction times and local heat transfer conditions [34–36].

In this paper, we proposed a 3D numerical model to study the influence of varying scanning speed on the quality of the 316L stainless steel solidified tracks and on the appearance of dynamic instabilities. For this, we have considered fixed laser power, beam radius, and powder thickness (130 W, 60  $\mu\text{m}$ , 40  $\mu\text{m}$ ) and variable scanning speeds (0.7; 0.9; 1.3; 1.5; 1.7;

**Fig. 1** The computational domain: enviroing air, powder bed, substrate (a), and its mesh (b)



1.9; 2.0 m/s). The Ansys Fluent software, which is a powerful numerical tool, was used to solve the Navier–stokes equations by including the phase change and the volume of fluid models.

## 2 Computational model and methodology

For our computational model, we considered a thin powder layer of stainless steel (40  $\mu\text{m}$ ) placed over a dense substrate of the same material (200  $\mu\text{m}$ ), (see Fig. 1a). The system is in an air protective atmosphere ( $T_0 = 300\text{ K}$ ,  $P_{\text{atm}} = 1\text{ atm}$ ). The thermal properties and the process parameters are listed in Table 2.

**Hypotheses** In order to simplify and solve the Navier–Stokes equations of our model, appropriate assumptions are listed below:

- The molten metal is assumed incompressible, Newtonian and laminar.
- Losses by radiation are neglected.
- Introduction of the Bousinesq approximation:  $\rho = \rho_0 - \beta(T - T_0)$ .
- Gaussian distribution of the laser with the fundamental mode ( $\text{TEM}_{00}$ ) is used.
- Thermal properties of the 316L stainless steel are assumed constant except for density and thermal conductivity, which are temperature dependent [37].

### Numerical method:

For this simulation, the computational domain was initially meshed by the pre-processor Gambit. The mesh size was adapted to provide thin cells in the interaction zone of the laser with the powder bed, where the gradients of temperature and velocity are important. The mesh size was increased in the substrate and air regions in order to reduce the computational time (Fig. 1b). The Cartesian mesh grid contains 520.000 hexahedral cells with non-uniform grid spacing. During the interaction between the laser beam and the powder bed, our model simulates the heat input from the laser

**Table 2** The thermo physical properties and the process parameters chosen in this simulation

Parameter	Value
Solidus temperature	1658 (K)
Liquidus temperature	1723 (K)
Enthalpy change of melting	$27 \times 10^4$ (J/Kg)
Absorption coefficient	0.45
Reflectivity	0.45
Solidus density	$f(T)$ ( $\text{kg}/\text{m}^3$ )
Powder density	$f(T)(1 - \epsilon)$ ( $\text{kg}/\text{m}^3$ )
Liquidus density	$f(T)$ ( $\text{kg}/\text{m}^3$ )
Thermal conductivity of solid	$f(T)$ (W/m. K)
Powder thermal conductivity	$f(T)(1 - \epsilon)$ ( $\text{kg}/\text{m}^3$ )
Thermal conductivity of liquid	$f(T)$ (W/m. K)
Specific heat	500 (J/Kg.K)
Viscosity	0.003 (Pa.s)
Surface tension	1.2 (N/m)
Thermo-capillary coefficient	$-0.43 \times 10^{-3}$ (N/m.K)
Laser power	130(W)
Scanning speed	0.7; 0.9; 1.3; 1.5; 1.7; 1.9; 2.0 (m/s)
Spot laser radius	60 ( $\mu\text{m}$ )
Powder layer thickness	40 ( $\mu\text{m}$ )
Porosity ( $\epsilon$ )	45%
Emissivity ( $\epsilon'$ )	0.4
Convective heat transfer coefficient	15 ( $\text{W}/\text{m}^2\text{K}$ )

to the powder. The laser beam scans area on the powder bed having the dimensions of (0.8 mm  $\times$  0.4 mm  $\times$  0.34 mm). Where the dimensions of the substrate, powder bed and air are given as follows: The substrate: (x:0.0, + 0.8; y:0.0, + 0.4; z:0.0, 0.2) mm; the powder bed: (x:0.0, + 0.8; y:0.0, + 0.4; z: 0.2, + 0.24) mm; the air: (x:0.0, + 0.8; y:0.0, + 0.4; z: + 0.24, + 0.34) mm.

The laser source heats and melts the metal powder selectively, and the two phases (air and powder bed) are initially

**Table 3** Comparison between the heat source and the radiative losses

Q (W/m <sup>2</sup> )	Qr (W/m <sup>2</sup> ) = $\sigma \epsilon (T^4 - T_0^4)$	Rr = Qr/Q
3.1e+9	4.59e+06	1.48e-03

both treated as incompressible fluids. The VOF method is used to track the interfaces between the gas and the metal phases (liquid/air interface and solid /liquid metal interface) during each time step. In each cell, the fraction of metal is (f) and the fraction of the air is (1-f). The phase change of the stainless steel from liquid to solid or from solid to liquid during the melting or cooling is treated by the 'Melting and Solidification' model. This model is implemented in Ansys-Fluent by an enthalpy based state change approach. The powder bed is then molten and rapidly solidified into a dense solid state, using the latent heat of fusion (270 kJ/kg). To deal with our volumetric laser source of energy term and some temperature dependent physical properties and surface tension, user defined functions (UDFs) written in C++ are included during the computing process.

The residuals of continuity and momentum equations convergence criteria are satisfied by applying as 10<sup>-4</sup> and 10<sup>-6</sup> for the energy equation. The assigned time step for this mesoscale simulation was 100 ns. The initial temperature of the powder and substrate were set to 300 K. In addition and at (t > 0), due to the relatively high thickness of the substrate (200 μm) and to the fast laser beam that do not allow heating the rear face up to a significant value, we can set the bottom of this later adiabatic. The boundary condition at the lateral surface of the powder bed or powder/air interface, is a heat exchange by conduction, which equalizes the loss by natural convection, it can be described as;  $k \frac{\partial T}{\partial n} = Q_c$ , with  $Q_c (Q_c = h_c (T - T_0))$ . The side and bottom boundaries are always in solid state, since melt fronts do not reach these boundaries so adiabatic and zero velocities are imposed. The air boundaries (top and sides) are always in atmospheric pressure since surface deformations do not touch these boundaries.

Our computational code [38, 39] was validated by comparing some of our results (when the Marangoni convection was included) with the experimental ones of Khairallah et al. [40, 41].

### 3 Governing equations

Ansys Fluent provides the capability of simulating the thermal aspect and the morphology of the obtained melt pool, and solves numerically the Navier–Stokes equations [42]. Based on the above assumptions, our conservation equations written in vector form will be reduced to:

$$\nabla \cdot V = 0 \tag{1}$$

$$\left( \frac{\partial(\rho V)}{\partial t} + \nabla \cdot (\rho V V) \right) = -\nabla p + \nabla \cdot (\mu \nabla V) + \rho_0 g - \rho_0 g (1 - \beta \Delta T) - \gamma k n \tag{2}$$

$$\frac{\partial \rho H}{\partial t} + \nabla \cdot (\rho V H) = (\nabla \cdot k (\nabla T)) + Q \tag{3}$$

In which ρ stands to density, t to the time,  $\vec{V}$  to the fluid velocity, p to the pressure, H represents the enthalpy and k the thermal conductivity. Additionally,  $\rho_0 \vec{g}$  denotes the gravity force,  $\gamma k \vec{n}$ , the surface tension force (capillary force), which is normal to the curvature of the interface between the molten pool and the air phase. The surface tension force is added as a source term to the momentum equation. In the second equation of the system, appears the buoyancy force:  $\rho_0 g (1 - \beta \Delta T)$ , which is dependent on the coefficient of thermal expansion β. In the case where the Marangoni convection was neglected, the natural convection becomes non-negligible.

For the phase change, we have used the 316 L stainless steel latent heat of fusion ( $L_f = 270$  kJ/kg), and the enthalpy H (J/m<sup>3</sup>). This latter can be written as  $H = \int_{T_0}^T \rho C dT$ , where ρ is the material density, C is the specific heat, and T the temperature of the molten pool formed in the powder bed. The beginning of melting is happened when the temperature is ranging between the solidus and liquidus temperatures ( $T_s, T_l$ ), so a liquid fraction α, is defined to indicate the level of melting. It ranges between zero (if  $T \leq T_s$ ) and one (if  $T \geq T_l$ ), with  $\alpha = \frac{T - T_s}{T_l - T_s}$ , ( $T_s < T < T_l$ ), so that  $\Delta H = \alpha L_f$ .

The laser heat source Q, was considered as volumetric (W/m<sup>3</sup>); it is added as a source term to the energy equation.

In the following, we focus on the occurrence of instabilities, on the temperature field and on the morphology of the solidified tracks obtained for different scanning speeds and when the laser source has travelled a fixed distance of 0.75 mm.

### 4 Results and discussion

During the scanning of the stainless steel powder, the laser beam spot center was initially located at point ( $x_i = 0.1$  mm,  $y_i = 0.2$  mm,  $z_i = 0.24$  mm) and then is moved along the X (+) direction for all our simulation conditions (Fig. 1a). A user defined function UDF is used to introduce the laser heat input, which describes the Gaussian distribution laser intensity given by:

$$Q(r) = q_0 \exp\left(-\frac{(x - x_i)^2 + (y - y_i)^2}{2(x_0^2 + y_0^2)}\right),$$

**Fig. 2** Surface morphology evolution of the tracks (a–g) and their corresponding temperature fields (h–n) at  $P = 130$  W and for different scanning speeds  $V = (0.7; 0.9; 1.3; 1.5; 1.7; 1.9; 2.0)$  m/s

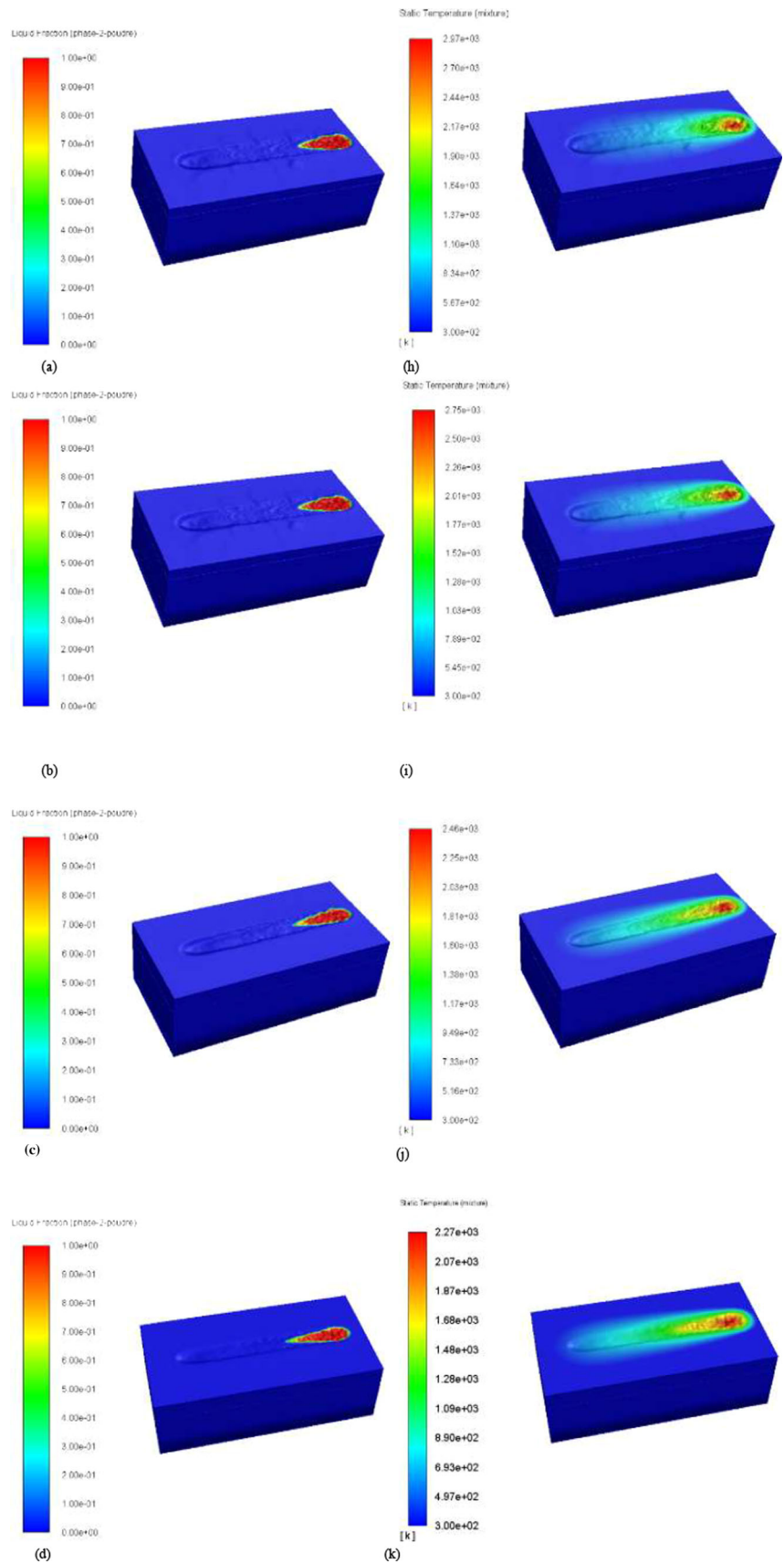
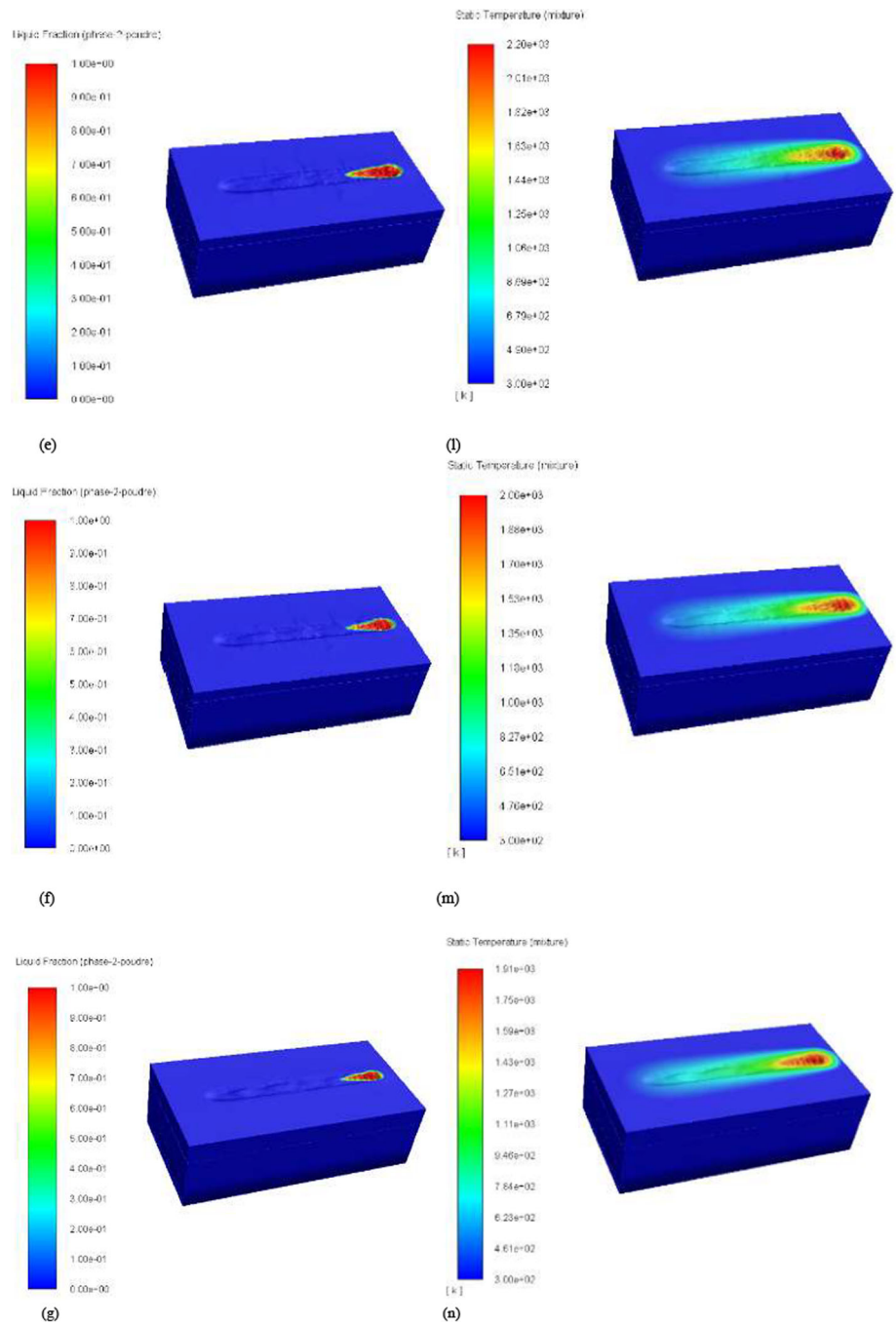


Fig. 2 continued



$$\text{with } q_0 = \frac{(1 - R)AP}{\pi(x_0^2 + y_0^2)e} \quad (4)$$

where R is the reflectivity of the stainless steel, A is its laser energy absorptivity and e is the layer thickness bed.  $R_0^2 = (x_0^2 + y_0^2)$ , is the square radius of the laser spot.  $r^2 = (x - xi)^2 + (y - yi)^2$ , is the square distance from a point on the powder bed surface. The Gaussian distribution laser beam is employed as a volumetric heat source on the interface between the air and metal powder phase, because it

is the suitable heat source to correctly simulate the process. In fact, the discontinuous mass distribution of particles in the powder bed requires the use of a volumetric heat source [43]. In this case, the laser intensity is extremely high at the center and lower gradually at the periphery. The heat absorbed by the powder is partially lost by convection, radiation and vaporization.

During the scanning, we have neglected the radiative losses. To justify this hypothesis, we calculated its ratio with

the input heat flux coming from the laser source for the highest temperature obtained in our simulation. This ratio is given in Table 3, where we can conclude that the radiative losses are negligible near the heat input.

Figures 2 depict the morphologies of the progressive solidification of the tracks (a, b, c, d, e, f, g), and the corresponding temperature fields (h, i, j, k, l, m, n) for the chosen scanning speeds ( $V = 0.7; 0.9; 1.3; 1.5; 1.7; 1.9; 2.0$  m/s) during the process. These tracks have a constant distance ( $x = 0.75$  mm =  $0.1 + V \cdot t$ ) traveled by the laser spot with different scanning speeds which implies different corresponding times.

While keeping some of the processing parameters constants ( $P = 130$  W,  $R_0 = 60$   $\mu$ m,  $e = 40$   $\mu$ m), we identified two major melt flow phenomena during our simulation. The first phenomenon that is observed involves ripples on the surface of the tracks. These ripples were related to the periodic oscillation of the molten pool. The tracks deemed irregular for the three following scanning velocities (0.7, 0.9, 1.3 m/s) (see Fig. 2a–c).

The irregular solidified tracks consist of approximately circular zones oriented perpendicular to the scanning direction and as the scanning speed increases, the ripples are further apart, and then their number becomes significantly lower. According to the literature and previous studies [20, 24, 25], the authors explain that the molten pool had periodic oscillations due to the recoil pressure that occurred at high input energy densities or at low scanning speeds. For them, these oscillations are responsible for the periodic change of the molten flow direction at the rear, which caused the formation of ripples during the process. However, in our present work, we have shown that this phenomenon can occur even in the absence of evaporation and recoil pressure. A further increase of the scanning speed (1.5 m/s) leads to the disappearance of these ripples, and the change of the track morphology, which becomes upwardly convex. Consequently, we can observe a peak at the center and a trough at the periphery of the track surface. In fact, as the molten pool cools, the normal component of the surface tension force increases, so the liquid metal will flow up during the scanning as shown in Fig. 3d. In this special case, the track is relatively smooth, continuous, and so stable.

A continuous increase in the scanning speed, namely  $V = (1.7; 1.9)$ , yields to a transition between a stable and an unstable melt-pool (called humping transition) which is called the pre-humping regime. The pre-humping regime presents elongated humps (see Figs. 3f and g). However, the humping regime obtained at the highest scanning speed (2.0 m/s) shows the occurrence of shorter and rounded humps. This periodic instability is accompanied by a thinner melt-pool flow, which provoke periodic shrinking effect (Fig. 3g). This shrinking effect indicates that the reason for this phenomenon is related to an insufficient energy input, since higher scanning speed leads to lower laser power absorption and then to

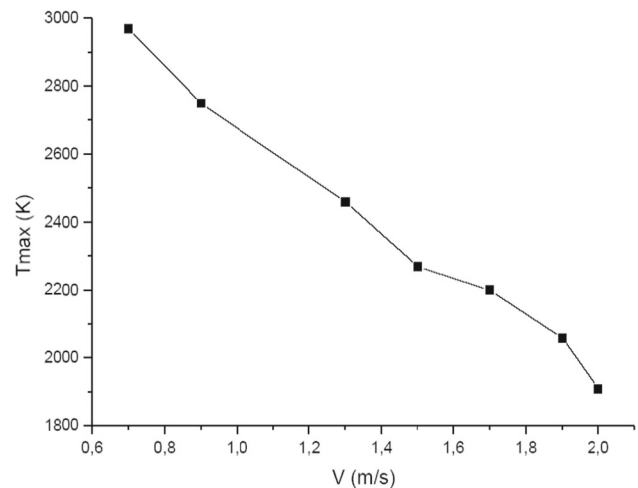


Fig. 3 Maximum temperature versus scanning speed

thinner melt pool. This tends to create greater contact angles, and the growth of perturbations of the molten track. Consequently, the slender and unstable molten metal leads to the occurrence of this periodic humping instability observed at a high scanning velocity. This phenomenon is usually attributed to Plateau–Rayleigh or Rayleigh–Taylor (RT) capillary instability. Additionally, we observe an accentuated tailing phenomenon at the rear of the molten pool as the scanning speed increases.

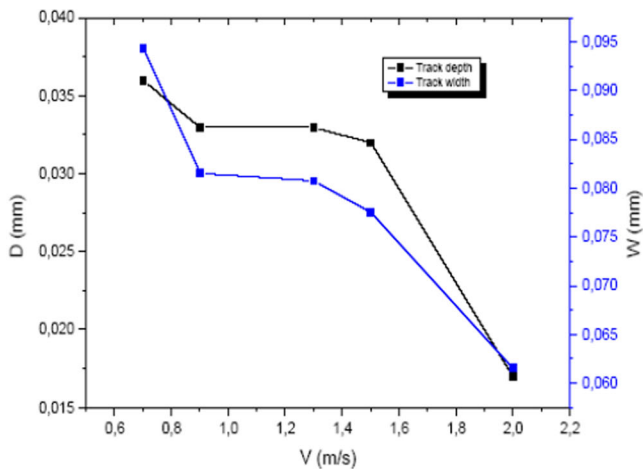
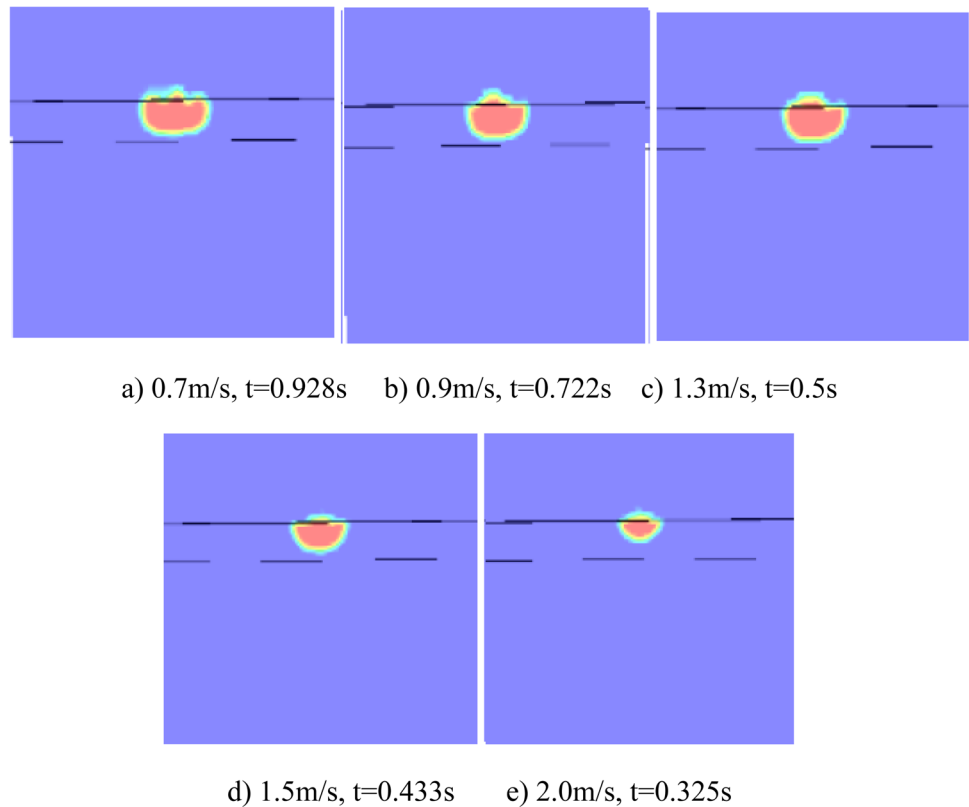
The figures (h, i, j, k, l, m, n) show how the temperature field tends to decrease with the increase of the scanning speed, since there is a reduce in the absorption of the laser beam, because the powder layer is exposed to the laser for less time. Moreover, higher temperatures are observed near the center of the laser spot on the other hand we observe an attenuation of the laser irradiation at the edges. The maximum temperature of the molten pool does not exceed the boiling point (3200 K), even at the lowest scanning speed (see Fig. 3), for this reason the radiation was neglected. We can then confirm that the energy density of the laser is really in the conduction mode and it is only enough to melt the metal.

Figure 4 show the transverse sections of the liquid fractions for the different scanning speeds (a: 0.7; b: 0.9; c: 1.3; d: 1.5; e: 2.0) m/s at the fixed distance  $x = 0.75$  mm and at their corresponding times (0.928; 0.722; 0.5; 0.433; and 0.325 s). These figures clearly show the quasi-semicircular geometry related to the conduction mode and the decrease in the liquid fraction as the scanning speed increases. The graphs of Fig. 5a, b give the depths, widths, lengths and heights of these molten fractions, where we notice a decrease as the scanning speed increases except for the length which presents fluctuations.

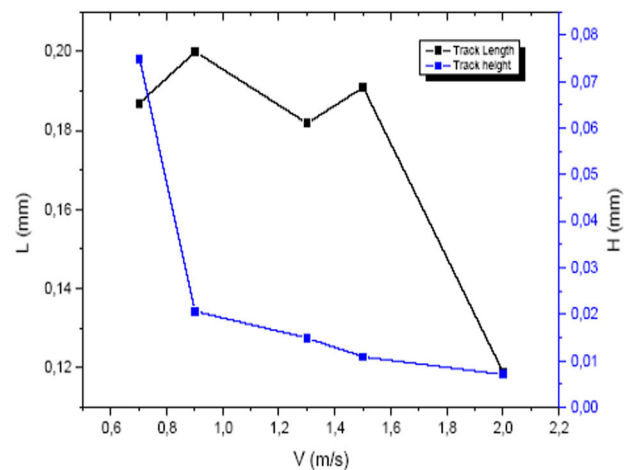
Figure 6 depicts the energy density  $De$  ( $J/m^2$ ) versus scanning speed (m/s). We can see at high energy densities and at



**Fig. 4** Transverse section of the liquid fractions at  $X = 0.75$  mm and for different scanning speeds  $V =$  (a: 0.7; b: 0.9; c: 1.3; d: 1.5; e: 2.0) m/s



(a)



(b)

**Fig. 5** Depth and width of the melt pool versus scanning speed (a), Length and height of the melt pool versus scanning speed (b) ( $P = 130$ W)

low scanning speeds the occurrence of ripples, on the other hand, and at low energy densities and high scanning speeds the occurrence of the prehumming and humping regimes. This has been already verified in both processes: selective laser melting and laser micro-welding processes [44–49].

It should be noted that, the solid line corresponding to 1.5 m/s where the melt stream is stable gives the transition between the two instabilities.

- Marangoni convection effect on the appeared instabilities:

In this sub section, we present the effect of Marangoni convection on the appeared instabilities. By introducing this convection, we must add into the above momentum equation the tangential Marangoni force, it will be written as:

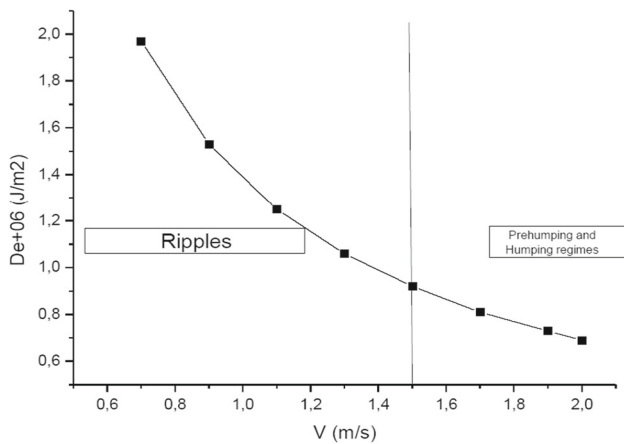


**Fig. 6** Energy density versus scanning speed, a transition between the two instabilities is shown at  $V = 1.5$  m/s

$$\left( \frac{\partial(\rho \mathbf{V})}{\partial t} + \nabla \cdot (\rho \mathbf{V} \mathbf{V}) \right) = -\nabla p + \nabla \cdot (\mu \nabla \mathbf{V}) + \rho_0 \mathbf{g} - \rho_0 \mathbf{g} (1 - \beta \Delta T) - \gamma \mathbf{k} \mathbf{n} + \frac{\partial \sigma}{\partial T} [\nabla T - \mathbf{n}(\mathbf{n} \cdot \nabla T)] \quad (2')$$

In which,  $\frac{\partial \sigma}{\partial T} \left[ \vec{\nabla} T - \vec{n} (\vec{n} \cdot \vec{\nabla} T) \right]$  : is the Marangoni shear force, which is tangential to the interface between the molten pool and the air phase. It is appeared because of surface tension difference due to the gradients of temperature on the molten pool surface (generated by the Gaussian distribution of the laser beam). The surface tension forces are added as a source term to the momentum equation.

In the SLM processes, the melt pools are predominantly driven by Marangoni convection, due to the laser Gaussian distribution, which yields to the temperature and surface tension gradients. This convection plays an important role in the energy transfer to the surrounding heat affected zone. We point out that heat Marangoni convection cannot be ignored in the conduction mode to accurately describe the melt pool morphology, and subsequently the solidified track. We have ignored it in the above discussion, just to simplify the numerical study and separate the influence of recoil pressure with the Marangoni convection effect.

Temperature gradient also leads to density gradient, which gives rise to buoyancy force, but when compared with Marangoni driven force, this latter is much high important. The Marangoni stresses are tangential forces, acting at the free surface, and they are due to the dependence of surface tension on temperature. They must be balanced by the shear stresses due to the liquid metal viscosity. Deformations of the free surface can occur when these surface tension forces cannot balance the shear forces during the scan process.

Since the thermo-capillary coefficient of the 316 L stainless steel is negative, then the Marangoni convection drives the flow from the hot regions (center) to the cold ones (periphery), and shear stresses drive it to the center. The outward flow along the free surface transports the heat from the hot surface to the cooler edges, thus reducing the maximum temperature observed initially when this convection was ignored (see Fig. 8 of temperature contours). Actually, the convective mixing gives agitation of melt pools, due to the tangential Marangoni shear stresses, which yield to a more unstable melt pools. This leads to disturbed ripples and humps as shown in Fig. 7 below (the last two figures are large in order to clearly show the humps).

In fact, during heating the tangential Marangoni force is the main driving force, which yields to a more unstable melt pools, however, during cooling this force attenuates and the normal surface tension force becomes more dominant and tends to flow up and to smooth the melt pool.

From the above results, it can be seen that the appearance of a uniform and smooth track is obtained for a higher scanning speed, namely 2.0 m/s. In this case, we need to go for larger scan speeds ( $V > 2.0$  m/s) to see if the humping instability reappears.

By increasing the scanning speed, we observed elongated humps at 2.1 and shorter and rounded ones at 2.2 m/s. We can say that, the transition between a stable melt pool and an unstable one (called humping transition) is observed in this case at  $V_s = 2.0$  m/s.

We must exclude the conclusion made by Wang et al. [27], which says that Marangoni convection is at the origin of the presence of ripples. Since we have demonstrated before that in the absence of this convection these ripples persist.

The top view of the temperature contours when Marangoni convection is introduced show reduced temperatures (see Fig. 8), and this can be detected by comparing the maximum temperature contours with those of the previous contours (without Marangoni). This reduction is due to the convection thermal agitation. It should be also noted that, during heating the thermal gradients are higher than those observed during cooling are.

## 5 Conclusion

**Conclusion:** A numerical model in the mesoscale was established to simulate the surface morphology and the temperature field during the scan of single line track for a given laser power, spot diameter and layer powder thickness in the selective laser melting process of the 316 L stainless steel material. Considering the influence of the scanning speed on the quality of the tracks, our simulation shows the occurrence of two dynamic instabilities. We identified ripples at low scanning speeds and humps at higher ones.

**Fig. 7** Surface morphology evolution of the tracks at different scanning speeds  $V = (0.7; 0.9; 1.3; 1.5; 2.0, 2.1; 2.2)$  m/s and when Marangoni convection is included

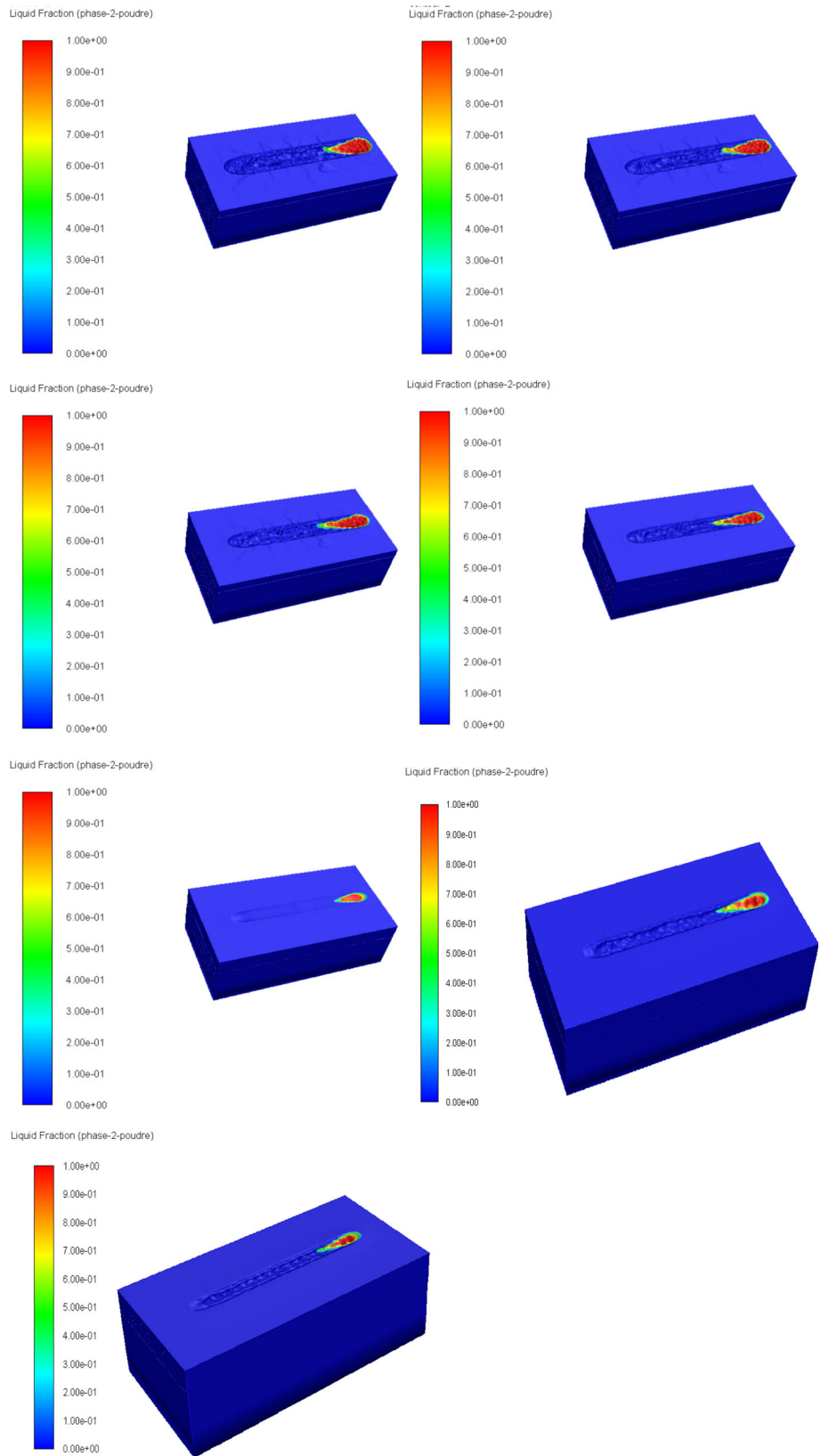
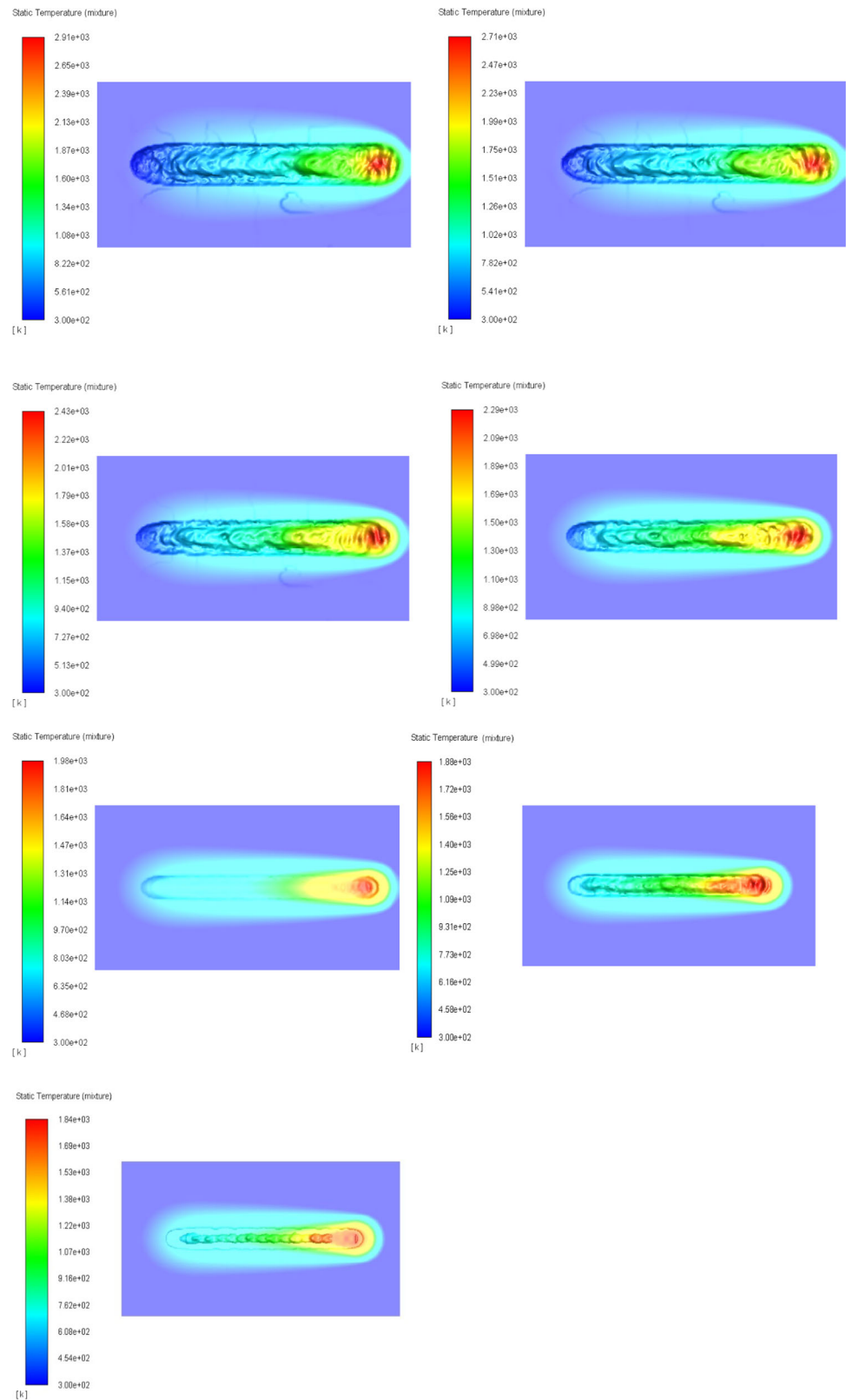


**Fig. 8** Top view of the temperature contours at different scanning speeds  $V = (0.7; 0.9; 1.3; 1.5; 2.0, 2.1; 2.2)$  m/s and when Marangoni convection is included



- We have concluded that, as the melt pool volume increases at low scanning speeds and when the normal component of the surface tension force exceeds the shear forces due to the liquid metal viscosity, the melt pool surface tends to ripple. These ripples become less and less apparent when the scanning speed increases, means the shear along the scanning direction becomes greater than the normal surface tension.
- We have also noticed the occurrence of pre-humping and humping regimes at higher scanning speeds. These regimes are related to a lack of melt pool, due to a low absorption of the energy input. The pre-humping regime presents elongated humps compared to those of the humping regime. This instability is characterized by thin melt pools, high surface tension coefficients and small melt-pool widths. It is usually attributed to Plateau–Rayleigh instability.
- In order to improve the quality of the manufactured tracks and consequently the produced parts, we try to prevent the occurrence of these instabilities by choosing suitable scanning speeds. we observed a stable state of the melt pool at 1.5 m/s, means at the transition between the two observed instabilities. We must clarify that, when we introduced the Marangoni convection, the stable state requires greater value to be achieved, namely 2.0 m/s.
- Finally, this numerical study allowed us to conclude that, ripples and humps are not systematically linked to the recoil pressure and Marangoni convection as expected by many researchers, since they can occur even when we remove the Marangoni convection and when the liquid steels are subjected to only conduction mode.

**Funding** The present research work has not received external funding.

**Data availability statement** The authors declare that the data supporting the findings of this study are available within the paper.

## Declarations

**Conflict of interest** The authors declare that they have no known competing financial interests or personal relationships that could have appeared to influence the work reported in this paper.

## References

- Kumar, L., Sharma, R.K.: Smart manufacturing and industry 4.0: state-of-the-art review. In: Handbook of Smart Manufacturing, pp. 1–28 (2023). <https://doi.org/10.1201/9781003333760-1>
- DebRoy, T., Wei, H.L., Zuback, J.S., Mukherjee, T., Elmer, J.W., Milewski, J.O., Beese, A.M., Wilson-Heid, A., De, A., Zhang, W.: Additive manufacturing of metallic components—process, structure and properties. *Prog. Mater. Sci.* **92**, 112–224 (2018)
- Ajay, M.R.K.: Incremental Sheet Forming Technologies: Principles, Merits, Limitations, and Applications. CRC Press, London (2020). <https://doi.org/10.1201/9780429298905>
- Kumar, A., Kumar, P., Srivastava, A.K., Goyat, V. (eds.): Modeling, Characterization, and Processing of Smart Materials. IGI Global, New York (2023)
- Kumar, A., Mittal, R.K., Haleem, A. (eds.): Advances in Additive Manufacturing: Artificial Intelligence, Nature-Inspired, and Biomanufacturing. Elsevier, New York (2022). <https://doi.org/10.1016/C2020-0-03877-6>
- Kumar, A., Mittal, R.K., Goel, R. (eds.): Waste Recovery and Management: An Approach Toward Sustainable Development Goals. CRC Press, London (2023). <https://doi.org/10.1201/9781003359784>
- Tang, H.P., Qian, M., Liu, N., Zhang, X.Z., Yang, G.Y., Wang, J.: Effect of powder reuse times on additive manufacturing of Ti–6Al–4V by selective electron beam melting. *JOM* **67**, 555–563 (2015). <https://doi.org/10.1007/s11837-015-1300-4>
- Kumar, A., Singh, H., Kumar, P., AlMangour, B. (eds.): Handbook of Smart Manufacturing: Forecasting the Future of Industry 4.0. CRC Press, London (2023). <https://doi.org/10.1201/9781003333760>
- Kumar, A., Kumar, P., Sharma, N., Srivastava, A.K. (eds.): 3D Printing Technologies: Digital Manufacturing, Artificial Intelligence, Industry 4.0. De Gruyter, New York (2024). <https://doi.org/10.1515/9783111215112>
- Aramian, A., Sadeghian, Z., Razavi, S.M.J., Prashanth, K.G., Berto, F.: Effect of selective laser melting process parameters on microstructural and mechanical properties of TiC–NiCr cermet. *Ceram. Int.* **46**(18, part A, 28), 749–28757 (2020). <https://doi.org/10.1016/j.ceramint.2020.08.037>
- Tolochko, N.K., Mozharov, S.E., Yadroitsev, I.A., Laoui, T., Froyen, L., Titov, V.I.M.B.: Ignatiev: balling processes during selective laser treatment of powders. *Rapid Prototyp. J.* (2004). <https://doi.org/10.1108/13552540410526953>
- Xiang, Y., Zhang, S., Wei, Z., Li, J., Wei, P., Chen, Z., Yang, L., Jiang, L.: Forming and Defect Analysis for Single Track Scanning in Selective Laser Melting of Ti6Al4V. *Appl. Phys. A Mater. Sci. Process* (2018). <https://doi.org/10.1007/s00339-018-2056-9>
- Liu, B.: Fuzzy process hybrid process and uncertain process. *J. Uncertain Syst.* **2**(1), 3–16 (2008)
- Liu, Y., Yang, Y., Mai, S., Wang, D., Song, C.: Investigation into spatter behavior during selective laser melting of AISI 316L stainless steel powder. *Mater. Des.* **87**, 797–806 (2015). <https://doi.org/10.1016/j.matdes.2015.08.086>
- Hamid, K.S., Parekh, S.G., Adams, S.B.: Salvage of severe foot and ankle trauma with a 3D printed scaffold. *Foot Ankle Int.* (2016). <https://doi.org/10.1177/1071100715620895>
- Zhang, D., Zhang, P., Liu, Z., Feng, Z., Wang, C., Guo, Y.: Thermofluid field of molten pool and its effects during selective laser melting (SLM) of Inconel 718 alloy. *Addit. Manuf. J.* **21**, 567–578 (2018). <https://doi.org/10.1016/j.addma.2018.03.031>
- Kempen, K.: Expanding the Materials Palette for Selective Laser Melting of Metals. KU Leuven, Belgium, Phd thesis (2015)
- Khairallah, S.A., Anderson, S.A.: Mesoscopic simulation model of selective laser melting of stainless steel powder. *J. Mater. Process. Technol.* **214**, 2627–2636 (2014). <https://doi.org/10.1016/j.jmatprotec.2014.06.001>
- Panwisawas, C., Qiu, C., Anderson, M.J., Sovani, Y., Turner, R., Attallah, M.M.: Mesoscale modelling of selective laser melting: thermal fluid dynamics and microstructural evolution. *Comput. Mater. Sci.* **126**, 479–490 (2017). <https://doi.org/10.1016/j.COMMATSCI.2016.10.011>

20. Voisin, T., Calta, N.P., Khairallah, S.A., Forien, J., Balogh, L., Cunningham, R.W.: Defects-dictated tensile properties of selective laser melted Ti–6Al–4V. *Mater. Des.* **158**, 113–126 (2018). <https://doi.org/10.1016/j.matdes.2018.08.004>
21. Zhou, X., Liu, X., Zhang, D., Shen, D., Liu, W.: Balling phenomena in selective laser melted tungsten. *Acta Mater.* **98**, 1–16 (2015). <https://doi.org/10.1016/j.jmatprot.2015.02.032>
22. Sun, J., Yang, Y., Wang, D.: Parametric optimization of selective laser melting for forming Ti6Al4V samples by Taguchi method. *Opt. Laser Technol.* **49**, 118–124 (2013). <https://doi.org/10.1016/J.optlastec.2012.12.002>
23. Chen, Z., Xiang, Y., Wei, Z., Li, J., Wei, P., Lu, B., Zang, L., Du, J.: Thermal dynamic behavior during selective laser melting of K418 superalloy: numerical simulation and experimental verification. *Appl. Phys. A* **124**, 1 (2018). <https://doi.org/10.1007/s00339-018-1737-8>
24. Zhang, J., Song, B., Wei, Q., Bourell, D., Shi, Y.: A review of selective laser melting of aluminum alloys: processing, microstructure, property and developing trends. *J. Mater. Sci. Technol.* **35**, 270–284 (2019). <https://doi.org/10.1016/j.jmst.2018.09.004>
25. Gecys, P.: Ripple formation by femtosecond laser pulses for enhanced absorptance of stainless steel. *J. Laser Micro Nanoeng.* **10**(2), 129–133 (2015). <https://doi.org/10.2961/jlmn.2015.02.0004>
26. Kou, S., Limmaneevichitr, C., Wei, P.S.: Oscillatory Marangoni flow: A fundamental study by conduction mode laser spot welding. *Weld. J.* **90**(20), 229–240 (2011)
27. Yang, T., Liu, T., Liao, W., Macdonald, E., Wei, H., Chen, X.: The influence of process parameters on vertical surface roughness of AlSi10Mg parts fabricated by selective laser melting. *J. Mater. Process. Technol.* **266**, 26–36 (2019). <https://doi.org/10.1016/j.jmatprotec.2018.10.015>
28. Wang, Z., Yan, W., Kam, W., Moubin, L.: Powder-scale multi-layer multi-track selective laser melting with sharp interface capturing method. *Comput. Mech.* **63**, 649–661 (2019). <https://doi.org/10.1007/s00466-018-1614-5>
29. Mumtaz, K., Hopkinson, N.: Top surface and side roughness of inconel 625 parts processed using selective laser melting. *Rapid Prototyp. J.* **15**, 96 (2009). <https://doi.org/10.1108/13552540910943397>
30. Antony, K., Arivazhagan, N., Senthilkumaran, K.: Numerical and experimental investigations on laser melting of stainless steel 316L metal powders. *J. Manuf. Process.* **16**(3), 345–355 (2014)
31. Gunenthiram, V., Peyre, P., Schneider, M., Dal, M., Frederic, C., Fabbro, R.: Analysis of laser-melt-pool-powder bed interaction during the selective laser melting of a stainless steel. *J. Laser Appl.* **29**, 022303 (2017). <https://doi.org/10.2351/1.4983259>
32. Seiler, M., Patschger, A., Bliedtner, J.: Investigations of welding instabilities and weld seam formation during laser microwelding of ultrathin metal sheets. *J. Laser Appl.* **28**, 022417 (2016). <https://doi.org/10.2351/1.4944446>
33. Gusarov, A.V., Smurov, I.: Modeling the interaction of laser radiation with powder bed at selective laser melting. *Phys. Procedia* **5**, 381–394 (2010). <https://doi.org/10.1016/j.phpro.2010.08.065>
34. King, W., Anderson, A.T., Ferencz, R.M., Hodge, N.E., Kamath, C., Khairallah, S.A.: Overview of modelling and simulation of metal powder bed fusion process. At Lawrence Livermore National Laboratory. *Mater. Sci. Technol.* **31**, 957–968 (2015)
35. Suryawanshi, J., Prashanth, K.G., Ramamurty, U.: Mechanical behavior of selective laser melted 316L stainless steel. *Mater. Sci. Eng. A* **696**, 113–121 (2017). <https://doi.org/10.1016/j.msea.2017.04.058>
36. Salman, O.O., Gammer, C., Eckert, J., Salih, M.Z., Abdulsalman, E.H., Prashanth, K.G., Scudino, S.: Selective laser melting of 316L stainless steel: influence of TiB<sub>2</sub> addition on microstructure and mechanical properties. *Mater. Today Commun.* **21**, 100615 (2019). <https://doi.org/10.1016/j.mtcomm.2019.100615>
37. Yadollahi, A., Shamsaei, N., Thompson, S.M., Seely, D.W.: Effects of process time interval and heat treatment on the mechanical and microstructural properties of direct laser deposited 316L stainless steel. *Mater. Sci. Eng. A* **644**, 171–183 (2015). <https://doi.org/10.1016/j.msea.2015.07.056>
38. Masmoudi, A., Bolot, R., Coddet, C.: Investigation of the laser–powder–atmosphere interaction zone during the selective laser melting process. *J. Mater. Process. Technol.* **225**, 122–132 (2015). <https://doi.org/10.1016/j.jmatprotec.2015.05.008>
39. Aggoune, S., Hamadi, F., Khelloufi, K., Tamsaout, T., Amara, E.H., Bougherara, K., Abid, C.: The Marangoni convection effect on melt pool formation during selective laser melting process. *Defect Diffus. Forum.* **412**, 107–114 (2021). <https://doi.org/10.4028/www.scientific.net/DDF.412.107>
40. Aggoune, S., Hamadi, F., Amara, E.H., Khelloufi, K., Tamssaout, T., Abid, C.: Effect of the radiative losses during selective laser melting process. *El Sevier Mater. Today Proc.* **53**(2341), 36–41 (2022). <https://doi.org/10.1016/j.matpr.2021.12.235>
41. Khairallah, S.A., Anderson, A.T., Rubenchik, A., King, W.E.: Laser powder-bed fusion additive manufacturing: physics of complex melt flow and formation mechanisms of pores, spatter, and denudation zones. *Acta Mater.* **108**, 36–45 (2016)
42. Ly, S., Rubenchik, A.M., Khairallah, S.A., Guss, G., Matthews, M.J.: Metal vapor micro-jet controls material redistribution in laser powder bed fusion additive manufacturing. *Sci. Rep.* **7**, 4085 (2017). <https://doi.org/10.1038/s41598-017-04237-z>
43. Lia, C.-J., Tsai, T.-W., Tseng, C.-C.: Numerical simulation for heat and mass transfer during selective laser melting of titanium alloys powder. *Phys. Procedia* **83**, 1444–1449 (2016). <https://doi.org/10.1016/j.phpro.2016.08.150>
44. Mishra, A.K., Aggarwal, A., Kumar, A., Sinha, N.: Identification of a suitable volumetric heat source for modelling of selective laser melting of Ti6Al4V powder using numerical and experimental validation approach. *Int. J. Adv. Manuf. Technol.* **99**, 2257–2270 (2018). <https://doi.org/10.1007/s00170-018-2631-4>
45. Yuan, W.H., Chena, H., Cheng, T., Wei, Q.: Effects of laser scanning speeds on different states of the molten pool during selective laser melting: Simulation and experiment. *Mater. Des.* **189**, 108542 (2020). <https://doi.org/10.1016/j.matdes.2020.108542>
46. Zhiheng, Hu., Balasubramanian Nagarajan, Xu., Song, R.H., Zhai, W., Wei, J.: Formation of SS316L single tracks in micro selective laser melting: surface, geometry, and defects. *Adv. Mater. Sci. Eng.* **2019**, 9 (2019). <https://doi.org/10.1155/2019/9451406>
47. Wang, J., Zhu, R., Liu, Y., Zhang, L.: Understanding melt pool characteristics in laser powder bed fusion: an overview of single- and multi-track melt pools for process optimization. *Adv. Powder Mater.* **2**, 100137 (2023). <https://doi.org/10.1016/j.apmate.2023.100137>
48. Gunenthiram, V., Peyre, P., Schneider, M., Dal, M., Coste, F., Fabbro, R.: Analysis of laser–melt pool–powder bed interaction during the selective laser melting of a stainless steel. *J. Laser Appl.* **29**, 022303 (2017). <https://doi.org/10.2351/1.4983259>
49. Patschger, A., Seiler, M., Bliedtner, J.: Influencing factors on humping effect in laser welding with small aspect ratios. *J. Laser Appl.* **30**, 032409 (2018). <https://doi.org/10.2351/1.5040620>

**Publisher's Note** Springer Nature remains neutral with regard to jurisdictional claims in published maps and institutional affiliations.

Springer Nature or its licensor (e.g. a society or other partner) holds exclusive rights to this article under a publishing agreement with the author(s) or other rightsholder(s); author self-archiving of the accepted manuscript version of this article is solely governed by the terms of such publishing agreement and applicable law.